Effects of Fracture Connectivity on Rayleigh Wave Dispersion

Gabriel E. Quiroga[1], J. Germán Rubino[2], Santiago G. Solazzi[1], Nicolás D. Barbosa[1], and Klaus Holliger[1]

[1]Institute of Earth Sciences, University of Lausanne, Switzerland.

[2]CONICET, Centro Atómico Bariloche - CNEA, San Carlos de Bariloche, Argentina.

Key Points:

- We study the impact of fracture density and connectivity changes on Rayleigh wave dispersion considering fluid pressure diffusion effects.
- We consider a stratified reservoir model in which a water-saturated fractured formation is represented following a poroelastic approach.
- Fracture connectivity, so far largely ignored, has a significant impact on Rayleigh wave dispersion, comparable to that of fracture density.

Corresponding author: Gabriel E. Quiroga, `Gabrielernesto.quiroga@unil.ch`

Abstract

Passive seismic characterization is an environmentally friendly method to estimate the seismic properties of the subsurface. Among its applications, we find the monitoring of geothermal reservoirs. One key characteristic to ensure a productive management of these reservoirs is the degree of fracture connectivity and its evolution, as it affects the flow of fluids within the formation. In this work, we explore the effects of fracture connectivity on Rayleigh wave velocity dispersion accounting for wave-induced fluid pressure diffusion (FPD) effects. To this end, we consider a stratified reservoir model with a fractured water-bearing formation. For the stochastic fracture network prevailing in this formation, we consider varying levels of fracture density and connectivity. A numerical upscaling procedure that accounts for FPD effects is employed to determine the corresponding body wave velocities. We use a Monte-Carlo-type approach to obtain these velocities and incorporate them in the considered fractured reservoir model to assess the sensitivity of Rayleigh wave velocity dispersion to fracture connectivity. Our results show that Rayleigh wave phase and group velocities exhibit a significant sensitivity to the degree of fracture connectivity, which is mainly due to a reduction of the stiffening effect of the fluid residing in connected fractures in response to wave-induced FPD. These effects cannot be accounted for by classical elastic approaches. This suggests that Rayleigh wave velocity changes, which are commonly associated with changes in fracture density, may also be related to changes in interconnectivity of pre-existing or newly generated fractures.

Plain Language Summary

Low-intensity seismic energy generated by natural or anthropogenic sources is used to obtain a number of physical properties of the subsurface. Amongst a wide range of applications, this technique is increasingly employed to characterize fractured geothermal reservoirs and to monitor their evolution. The interconnectivity of fractures is a critical characteristic of such reservoirs as it enables preferential pathways for fluid flow. Conventional models for interpreting such seismic data are based on linear elasticity and cannot account for realistic effects related to the interactions of pore fluid pressure and fracture connectivity. To alleviate this problem, we employ an advanced model that accounts for these so-called wave-induced fluid pressure diffusion (FPD) effects. We find that changes in the connectivity of fractures have a significant impact on seismic surface wave recordings. This opens the perspective of using such observations to monitor the hydraulic evolution of fractured reservoirs during successive production and stimulation cycles.

1 Introduction

Fractured rock formations are of increasing interest and importance for a wide range of applications throughout the Earth, environmental, and engineering sciences. Fractures tend to constitute preferential pathways for fluid flow and, as such, the hydraulic properties of a formation are greatly affected by the presence and connectivity of fractures. This, in turn, manifests itself in the need of new methods and techniques to detect fractures and characterize their geometrical, mechanical, and hydraulic properties. In this context, the use of passive seismic sensing to monitor the evolution of fracture networks has established itself due to its efficiency, reliability, and non-invasive nature. Prominent examples of scenarios where this technique has proven to be valuable include the monitoring of volcanic activity (e.g., Brenguier et al., 2008; Obermann et al., 2013), CO_2 sequestration (e.g., Boullenger et al., 2015; Gassenmeier et al., 2014), and geothermal energy production (e.g., Calò et al., 2013; Obermann et al., 2015; Taira et al., 2018).

Passive seismic methods comprise a vast range of approaches and techniques which employ the energy of naturally occurring seismicity to gain information of the subsurface. In active seismic regions, the energy released from natural earthquakes in the area can be used for this purpose. This method is known as local earthquake tomography (LET) (e.g., Aki & Lee, 1976; Thurber, 1983). Conversely, ambient-noise correlation or passive seismic interferometry is a passive seismic method based on surface wave analysis which is also applicable outside seismically active zones. Ambient-noise correlation is based on the inversion of Rayleigh wave velocity dispersion inferred from ambient seismic noise measurements to obtain S-wave velocity profiles of the studied zone. Even though this method initially started with pioneering works focused at the continental and regional scale (e.g., Campillo & Paul, 2003; Shapiro & Campillo, 2004), it quickly evolved towards smaller scales, proving its effectiveness as an exploration and monitoring tool for applications such as, for example, nuclear waste storage and CO_2 sequestration, which naturally target zones with low natural seismicity(Planès et al., 2020). Notably, this technique was employed successfully in the characterization of geothermal reservoirs by employing time lapse observations. Obermann et al. (2015) employed ambient-noise correlation in order to monitor the geothermal site of St. Gallen in Switzerland, which permitted the identification of aseismic perturbations associated with gas infiltration. More recently, Taira et al. (2018) used ambient-noise correlation to monitor the response of the Salton Sea geothermal site in the U.S.A. to fluid extraction and local earthquake activity. Interestingly, these authors attributed observed surface wave velocity reductions to the opening of preexisting fractures due to induced stresses. In addition to this, it can be expected that fluid pressure diffusion (FPD) effects play a role in this scenario, as in the presence of fluid saturated fractures, such poroelastic effects have a significant impact on the effective mechanical properties of the medium in response to seismic waves (e.g., Rubino et al., 2013, 2014, 2017). To date, surface wave analyses do not, however, account for wave-induced FPD.

When seismic waves travel through a fluid-saturated porous medium containing a distribution of mesoscopic fractures, that is, fractures larger than the typical pore size but much smaller than the prevailing seismic wavelengths, fluid pressure gradients are induced between compliant fractures and the stiffer embedding background, as well as between connected fractures (e.g., Rubino et al., 2013, 2014). The consequent pressure equilibration processes, usually referred to as fracture-to-background (FB) and fracture-to-fracture (FF) FPD, result in a frequency dependence of the effective mechanical moduli of the medium. The prevalence of these mechanisms is dependent on the frequency of the seismic waves. In low-permeability formations and in presence of centimeter- to meter-scale fractures, FB-FPD typically prevails at frequencies below the seismic frequency range ($\lesssim 0.01$ Hz), while FF-FPD occurs at frequencies above the seismic frequency range ($\gtrsim 10^3$ Hz). The effects of FPD on body wave velocities of fractured rocks were extensively studied, and it was demonstrated that the density, connectivity and orientation of fractures have a significant impact on the phase velocity dispersion and attenuation as well as on the anisotropy of body wave velocities (e.g., Gurevich et al., 2009; Vinci et al., 2014; Rubino et al., 2017; Solazzi et al., 2020). However, the corresponding impact on surface wave properties, such as, for example, their velocity dispersion characteristics, in the context of subsurface exploration and monitoring settings remains largely unexplored. Previous works associate surface wave velocity decreases in seismically active environments with the opening of fractures and the associated increases of fracture density (e.g., Silver et al., 2007; Taira et al., 2015, 2018). However, this interpretation ignores the possibility that changes in the fracture density may also be associated with changes in the connectivity between fractures and disregards the associated FPD effects on the properties of surface waves.

The aim of this work is to explore the importance of fracture-related FPD effects on surface wave velocity dispersion. Our main objective is to better understand the effects that fractures in general, and their interconnectivity in particular have on this widely used observable. The paper proceeds as follows. We begin by explaining the method used to compute synthetic Rayleigh wave dispersion curves in elastic layered media. We then outline of the theoretical basis of poroelasticity and the associated upscaling procedure employed to compute the effective seismic properties of fractured formations. Then, we consider a canonical model to explore the effects of FPD for a wide range of pertinent parameters, which allow us to systematically explore the effects of fracture density and interconnectivity on Rayleigh wave phase and group velocities. To assure the representativity of our results, we use a Monte Carlo approach to explore the corresponding parameter space. Rayleigh wave dispersion curves are analyzed for fracture distributions characterized by constant and variable length in order to determine if the multiplicity of scales prevailing in many natural settings has significant impact on the results.

2 Methodology

2.1 Rayleigh Wave Dispersion

Rayleigh waves propagate along the Earth's free surface as a superposition of P-waves and vertically polarized S-waves. They are characterized by a counter-clockwise elliptical particle motion, whose amplitude decays exponentially with distance from the free surface. Conversely, geometrical spreading effects are very small compared to those of body waves, and, hence, Rayleigh waves tend to be prevalent in seismic recordings (e.g., Stein & Wysession, 2003). In a stratified medium with varying seismic velocities, Rayleigh wave propagation is dispersive, which manifests itself in a prominent frequency dependence of their phase velocities. The reason for this is that different frequencies are associated with different wavelengths and, thus, with different sensitivity to depth. Correspondingly, passive seismic approaches allow to characterize the subsurface through the inversion of Rayleigh wave dispersion curves extracted from ambient noise records (e.g., Socco et al., 2010; Wang & Yao, 2020).

We consider a layered medium whose axis of symmetry is normal to the surface and impose the following boundary conditions for waves travelling in a layered half-space in contact with a free surface: (i) no stress at the surface; (ii) no stress and strain at infinite depth; (iii) continuity of stress and displacements at layer interfaces; (iv) plane strain field. In this context, the equation of motion can be written as a linear differential eigenvalue problem (e.g., Aki & Richards, 1980)

$$\frac{d\mathbf{f}(z)}{dz} = \mathbf{A}(z)\mathbf{f}(z), \tag{1}$$

where $\mathbf{f}$ is a vector composed of two displacement eigenfunctions and two stress eigenfunctions, $\mathbf{A}$ is a 4x4 matrix depending on the vertical distribution of the of the subsurface properties and z is the vertical coordinate. Equation 1 has nontrivial solutions for certain values of the wavenumber. The associated equation is known as the Rayleigh secular equation and in its implicit form is given by (e.g., Socco et al., 2010)

$$F_R[\lambda(z), G(z), \rho(z), k_j, f] = 0, \tag{2}$$

where λ and G are the Lamé parameters, ρ is the density, k_j is the wavenumber of the mode of propagation j, and f is the frequency. The variables corresponding to the material parameters of the subsurface depend on z. For a stratified medium where each layer has homogeneous mechanical properties, this problem can be expressed using a matrix formulation, as shown by the works of Thomson (1950) and Haskell (1953). These authors introduced the so-called matrix propagator method which conceptualizes the subsurface as a stack of layers overlying a semi-infinite half-space. These algorithms are commonly employed for the computation of Rayleigh wave dispersion curves for a wide variety of applications. Buchen and Ben-Hador (1996) provide a review of the most significant propagator matrix algorithms and introduce the so-called "fast delta matrix" method, which we use in this study. The procedure to determine the associated Rayleigh wave phase and group velocities consists of finding the roots of the Rayleigh secular equation (Equation 2), for which we use the secant method (e.g., Press et al., 1986). The fast delta matrix method employed here provides exact solutions for models consisting of a stack of horizontal, elastic, and isotropic layers.

The objective of this work is to assess the effects of FPD in porous media containing fracture networks on Rayleigh wave dispersion. To this end, we will consider a layered subsurface model in which one of the layers represents a fractured formation. In this context, various scenarios of fracture connectivity are considered for Rayleigh wave dispersion modelling. The effective body wave velocities of the fractured formation required to compute Rayleigh wave dispersion are obtained by employing a numerical upscaling procedure, which is described in the following section.

2.2 Effective Body Wave Properties of Fractured Rocks in a Poroelastic Context

In the following, we briefly describe the effects of FPD on the seismic signatures of fractured rocks. This is followed by a brief review of Biot's poroelasticity theory (Biot, 1962), which is subsequently employed to model FPD effects in fractured porous media. To do so, we employ the numerical upscaling procedure proposed by Rubino et al. (2016), which was recently implemented into a versatile finite-element package named "Parrot" and allows to consider stochastic fracture distributions of realistic complexity (Favino et al., 2020).

2.2.1 Fluid Pressure Diffusion Effects

When a seismic wave propagates through a fluid-saturated porous medium containing fractures in the mesoscopic scale range, FPD affects its phase velocity and amplitude. In presence of connected fractures, two manifestations of FPD can arise (Rubino et al., 2013): one is governed by FPD between compliant fractures and their stiffer embedding background and is referred to as FB-FPD; the other is associated with FPD between connected fractures and is referred to as FF-FPD. Figures 1a to 1c show a representative rock sample of a medium of interest being subjected to harmonic displacements applied on its boundaries, which allow us to obtain the associated effective frequency-dependent elastic moduli (Rubino et al., 2016). Figures 1d to 1g show schematic illustrations of FPD effects in terms of the pressure distribution in a subsection of a fractured sample subjected to vertical compression (Figure 1a), which emulates the strains produced by a vertically travelling P-wave. Orange-colored regions of the medium denote the fluid pressure build-up created by the harmonic deformation and black arrows indicate the direction of the corresponding wave-induced fluid flow. The large stiffness contrast between fractures and background generates pressure gradients in response to the propagation of a seismic wave, which, in turn, generate oscillatory fluid flow between these regions and, thus, energy dissipation and velocity dispersion due to FB-FPD (Figure 1d). Figure 1f illustrates FF-FPD, where fluid flow and, thus, velocity dispersion and attenuation, is caused by local fluid pressure gradients occurring between intersecting fractures. Above the frequency range at which FF-FPD prevails, the sample behaves as if fractures were hydraulically isolated. This is the so-called no-flow limit, beyond which the medium essentially behaves elastically (Figure 1g). As mentioned before, for crystalline rocks, FB-FPD falls below the frequencies typical of passive seismic surveys, while FF-FPD corresponds to frequencies higher than those of passive seismics. As illustrated in Figure 1e, between these regimes we find a frequency range characterized by pressure equilibrium between connected fractures, which substantially reduces the stiffening effect of the fracture fluid compared to the elastic case. Figure 1h then presents an illustration of the associated body wave phase velocity as a function of frequency for samples containing connected and unconnected fractures. The FB-FPD and FF-FPD dispersion ranges are highlighted in yellow. For frequencies higher than the FB-FPD regime and lower than the FF-FPD regime, there is a non-dispersive plateau in which the medium behaves effectively as being elastic. Although there is neither attenuation nor velocity dispersion in this frequency range, FPD effects in presence of connected fractures produce a significant velocity drop. This means that, even though the body wave velocities in the plateau are representative of an elastic medium, this velocity change can only be modelled in the context of the theory of poroelasticity. For many applications of interest, the frequency range of approximately 0.1 to 10 Hz, at which passive seismic surveys are usually carried out (e.g., Obermann et al., 2015; Taira et al., 2018) is within the limits of this non-dispersive plateau. This implies that, as long as the frequencies considered correspond to those of the non-dispersive plateau, an elastic modelling such as the one described in Section 2.1 can be employed to evaluate Rayleigh wave dispersion in layered media.

2.2.2 Numerical Upscaling Procedure

The direct numerical simulation of FPD effects on wave propagation is a complicated task. This is mainly due to the fact that the dominant scales at which FPD takes

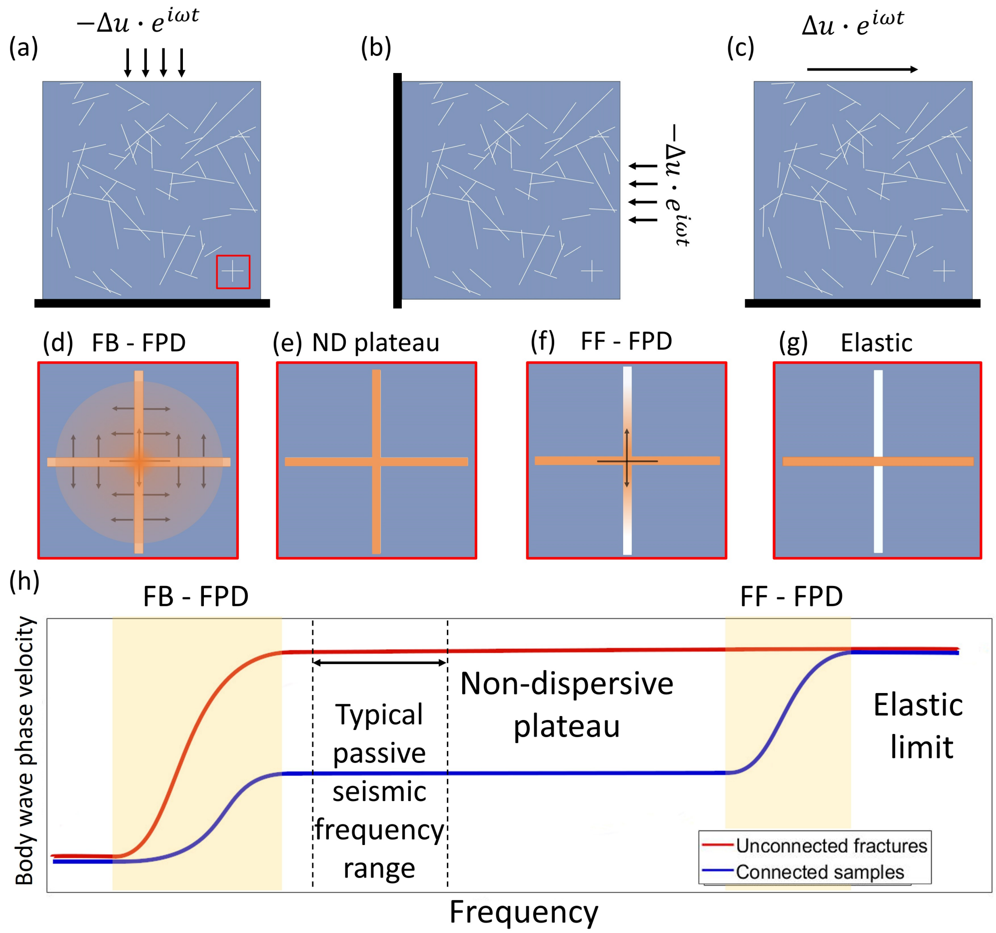

Figure 1. Schematic illustration of the (a) vertical, (b) horizontal, and (c) shear numerical oscillatory relaxation tests employed to obtain the equivalent stiffness matrix of the considered sample. (d, e, f, g) Fluid pressure distributions in a subsection of the sample highlighted in (a) subjected to a vertical compression for different dispersion regimes. Increasing pressure is denoted by progressive intensities of orange. (d) FB-FPD: pressure exchange between fractures and background rock, (e) non-dispersive (ND) plateau: pressure is equilibrated between connected fractures; (f) FF-FPD: pressure exchange between connected fractures; (g) elastic equivalent case: pressure confined to the horizontal fracture. (h) P- and S-wave velocities as functions of frequency for samples with unconnected fractures (red line) and connected fractures (blue line). The frequency ranges where body wave dispersion due to FB-FPD and FF-FPD prevails are highlighted in yellow. Typical frequency range of passive seismic studies is shown inside the ND plateau.

place are much smaller than the seismic wavelengths (Rubino et al., 2016). For this reason, numerical upscaling procedures are commonly employed to achieve an effective characterization of heterogeneous poroelastic media. In order to obtain the effective upscaled seismic response of a medium of interest, we solve Biot's equations for a so-called representative elementary volume (REV) of the medium. An REV is defined as a subvolume that is structurally typical of the whole medium and for which the inferred properties are independent of the applied boundary conditions (e.g., Milani et al., 2016). Fractures are conceptualized as highly porous, permeable, and compliant inclusions embedded in a much stiffer and much less porous permeable background (e.g., Nakagawa & Schoenberg, 2007). As seismic attenuation and velocity dispersion due to FPD are governed by fluid pressure gradients, we can neglect inertial terms (e.g., Rubino et al., 2013). Hence, Biot's poroelastic equations of motion (Biot, 1956b, 1956a) reduce to the so-called consolidation equations (Biot, 1941), which, in the space-frequency domain are given by

$$\nabla \cdot \boldsymbol{\sigma} = 0, \tag{3}$$

$$\nabla p_f = -i\omega \frac{\eta}{\kappa} \mathbf{w}, \tag{4}$$

where $\boldsymbol{\sigma}$ is the total stress tensor, p_f the pore fluid pressure, η the fluid viscosity, κ the permeability, ω the angular frequency, and $\mathbf{w}$ the relative fluid-solid displacement. These equations are coupled by the stress-strain constitutive relations (Biot, 1962)

$$\boldsymbol{\sigma} = 2\mu_m \boldsymbol{\epsilon} + \mathbf{I}(\lambda_c \nabla \cdot \mathbf{u} - \alpha M \xi), \tag{5}$$

$$p_f = -\alpha M \nabla \cdot \mathbf{u} + M\xi, \tag{6}$$

where $\mathbf{I}$ is the identity matrix, $\mathbf{u}$ the solid displacement, and $\xi = -\nabla \cdot \mathbf{w}$ a measure of the local change in the fluid content. The strain tensor is given by $\boldsymbol{\epsilon} = \frac{1}{2}(\nabla \mathbf{u} + (\nabla \mathbf{u})^T)$, where the superscript T denotes the transpose operator. The Biot-Willis parameter α, the fluid storage coefficient M, and the Lamé parameter λ_c are given by

$$\alpha = 1 - \frac{K_m}{K_s}, \tag{7}$$

$$M = \left(\frac{\alpha - \phi}{K_s} + \frac{\phi}{K_f} \right)^{-1}, \tag{8}$$

and

$$\lambda_c = K_m + \alpha^2 M - \frac{2}{3}\mu_m, \tag{9}$$

where ϕ denotes the porosity, μ_m the shear modulus of the bulk material, which is equal to that of the dry frame, and K_f, K_s, and K_m are the bulk moduli of the fluid phase, the solid grains, and the dry matrix, respectively. Please note that the dry frame modulus K_m is related to the undrained saturated modulus K_u through Gassmann's equation $K_m = K_u - \alpha^2 M$ (Gassmann, 1951). Due to computational constrains, we employ a 2D characterization for our medium under the hypothesis of plane strain conditions. The plane strain assumption implies that the considered fractures are long enough in the direction perpendicular to the considered plane of wave propagation to neglect pressure gradients, as well as normal and shear strains along this direction. This also implies that the seismic waves are assumed to propagate along the plane of the sample. In order to characterize the full stiffness matrix of a 2D medium, we apply three oscillatory relaxation tests to a corresponding REV, whose boundary conditions are illustrated in Figure 1. The first test consists of a harmonic vertical compression (Figure 1a), performed by applying a time-harmonic homogeneous vertical displacement at the top boundary of the representative sample, while keeping the vertical displacement of the sample null at the bottom boundary. The second test is a harmonic horizontal compression test (Figure 1b) and consists on applying a normal displacement at a lateral boundary of the sample, while keeping the horizontal displacement null at the opposing boundary. The third and final test consist of applying a harmonic horizontal displacement at the top boundary of the sample, while keeping the bottom boundary fixed in place (Figure 1c). Following Favino et al. (2020), the displacements and pressures obey periodic boundary conditions unless stated otherwise.

Given that a heterogeneous poroelastic medium can be represented by an effective homogeneous viscoelastic solid (e.g., Rubino et al., 2016; Solazzi et al., 2016), the volumetric average of stress and strain, in response to the three tests, can be related through an equivalent frequency-dependent and anisotropic stiffness matrix (Rubino et al., 2016)

$$\begin{pmatrix} \langle\sigma_{11}(\omega)\rangle \\ \langle\sigma_{22}(\omega)\rangle \\ \langle\sigma_{12}(\omega)\rangle \end{pmatrix} = \begin{pmatrix} C_{11} & C_{12} & C_{16} \\ C_{12} & C_{22} & C_{26} \\ C_{16} & C_{26} & C_{66} \end{pmatrix} \begin{pmatrix} \langle\epsilon_{11}(\omega)\rangle \\ \langle\epsilon_{22}(\omega)\rangle \\ \langle 2\epsilon_{12}(\omega)\rangle \end{pmatrix}, \tag{10}$$

where $C_{ij}(\omega)$ are the components of the equivalent stiffness matrix in Voigt notation, and $\langle\epsilon_{ij}(\omega)\rangle$ and $\langle\sigma_{ij}(\omega)\rangle$ represent the volume-averages of the strain and stress components, respectively. A least-squares procedure is employed to obtain the best-fitting values of C_{ij} using the averaged stress and strain fields obtained from the three tests for each frequency. The resulting P- and S-wave phase velocities are angle- and frequency-dependent, and are given by (Rubino et al., 2016):

$$V_{P,S}(\omega, \theta) = \frac{\omega}{\Re(\kappa_{P,S}(\omega, \theta))}, \tag{11}$$

where $\Re$ is the real part operator, $\kappa_{P,S}(\omega, \theta)$ denotes the complex-valued wavenumbers obtained by solving the elastodynamic equation in a medium defined by the stiffness matrix in equation (10). The reader is referred to the works of Rubino et al. (2016) and Favino et al. (2020) for the details of this upscaling procedure.

It is important to mention that these upscaling procedures allow us to obtain representative values of the rock physical properties of interest as long as the considered samples constitute an REV of the lithological unit of interest. In the presence of stochastic fracture distributions, identifying subvolumes that fulfill the criteria of an REV tends to be impractical due to the excessively large size of the samples that would be required for this purpose. To overcome this difficulty, we follow the approach of Rubino et al. (2009), who employ the previously outlined upscaling procedure in a Monte Carlo fashion on sub-REV-size samples. For this, we assume that the rock physical properties of the lithological unit of interest are statistically ergodic, and thus, stationary, such that spatial averages can be replaced by ensemble averages inferred through compressibility and shear tests to a multitude of random samples. This approach is equivalent to considering repeated applications of the upscaling procedure to randomly chosen samples as a repeated measurement of the rock physical properties of the lithological unit of interest. As such,

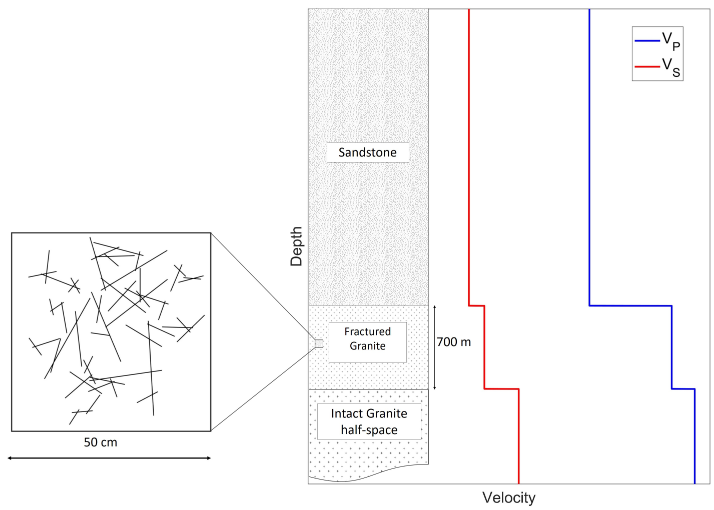

Figure 2. Schematic illustration of the canonical 1D model considered in this study showing the lithological column and the associated P- (blue) and S-wave (red) velocity profiles.The blow-up illustrates its detailed structure at the size of the samples considered in our upscaling procedure.

the representative mechanical properties can then be characterized by the corresponding mean values and variances inferred from a sufficiently large set of such measurements. Finally, please note that, while the velocities computed using the upscaling technique are in general frequency-dependent, in this work, we consider a frequency range in which the resulting velocities have no velocity dispersion.

3 Results

3.1 Numerical Framework

In order to assess the sensitivity of Rayleigh wave dispersion with regard to the effects of fractures in general and their interconnectivity in particular, we consider a canonical model composed of two horizontal layers overlying a half-space (Figure 2). The surficial layer corresponds to a 2500-m-thick sandstone formation, followed by a layer of fractured granite with a thickness of 700 m, and an underlying half-space consisting of intact granite. The sandstone layer is homogeneous and, hence, seismic waves traversing it are not attenuated or dispersed due to FPD effects. Its seismic properties are: $V_P = 3500$ m/s, $V_S = 2000$ m/s, and $\rho = 2500$ kg/m^3 (Mavko et al., 1998). For the fractured granite layer, the fractures are represented using highly porous and permeable inclusions. As mentioned above, we assume the statistical stationarity of the properties of the formation, which allows us to carry out the upscaling procedure previously described. This layer is characterized by its fracture density, quantified as the ratio of fracture area over the sample area, the length distribution of fractures, and the number of connections between fractures. These parameters have a significant impact on the resulting body wave velocities of saturated fractured samples (e.g., Hunziker et al., 2018). The underlying granitic half-space has the same material properties as the intact parts of the fractured granitic layer. As the surficial sandstone layer, it is homogeneous and hence devoid of FPD effects. The P- and S-wave velocities of this layer are computed as $V_P = \sqrt{\frac{K_u + 4/3\mu_m}{\rho_b}}$ and $V_S = \sqrt{\frac{\mu_m}{\rho_b}}$, respectively, where ρ_b is the bulk density of the medium. Note that one could alternatively obtain these velocities applying the upscaling procedure in the homogeneous layer. The physical properties of the granitic rocks and fractures are listed in Table 1. The granite properties correspond to those in Detournay and Cheng (1993) and the fracture and fluid properties to those from Rubino et al. (2017). The saturating pore fluid is brine, and the grain-level properties of the fractures are assumed to be consistent with those of the intact granite.

In order to estimate the body wave velocities of the fractured layer, we follow the upscaling procedure described in Section 2.2 employing isotropic rock samples with homogeneously oriented fractures. To explore the role played by the connectivity of the fractures, we consider two end-member-type scenarios: (i) fully connected and (ii) entirely unconnected fracture distributions. When generating a particular synthetic fractured sample, the center positions of the fractures are assigned randomly and fractures not meeting the stipulated connectivity criteria are substituted. This process is repeated until the desired fracture density is obtained and fractures are either fully connected or fully un-

Table 1.

Properties of intact granitic background rock and embedded fractures.

Property	Background	Fracture
Solid grain density	2700 kg/m^3	2700 kg/m^3
Solid grain bulk modulus	45 GPa	45 GPa
Dry frame shear modulus	19 GPa	0.02 GPa
Dry Frame bulk modulus	35 GPa	0.04 GPa
Permeability	1e-19 m^2	1e-10 m^2
Porosity	0.02	0.8
Fluid viscosity	1e$-$3 Pa.s	1e$-$3 Pa.s
Fluid bulk modulus	2.25 GPa	2.25 GPa
Fluid density	1090 kg/m^3	1090 kg/m^3

Note. Embedding background is assumed to correspond to intact granite (Detournay & Cheng, 1993). The pore fluid properties correspond to brine. Fractures are represented as highly compliant, porous, and permeable inclusions, whose grain-level properties correspond to those of the embedding background (Rubino et al., 2017).

connected. To avoid that the substitution process generates preferential orientations of the fractures, the original orientations are retained during substitution. For each connectivity scenario we consider three fracture densities: 0.25%, 0.50%, and 0.75%. These values were chosen based on the feasibility of generating completely connected and unconnected distributions. Finally, we consider two cases of fracture length distributions. We begin with fractures of constant length, in order to isolate the effects of fracture connectivity from those associated with fracture length variation. Later, we repeat the analysis considering a more realistic scenario where fractures have varying lengths governed by a power law distribution, which allows us to assess the impact of effects related to fracture geometry. Recall that, in order to compute effective P- and S-wave velocities for a given fracture density and connectivity, we employ a Monte-Carlo-type approach in combination with the upscaling procedure. The corresponding convergence criterion is based on the stability of the standard deviation (Rubino et al., 2009). The convergence analysis of the Monte Carlo approach is performed for a frequency of 1 Hz, which is typical of Rayleigh waves in passive seismic studies and is located within the non-dispersive plateau illustrated in Figure 1. As mentioned before, the fact that the frequencies of interest for Rayleigh wave monitoring fall within the non-dispersive plateau allows us to employ a purely elastic modelling of Rayleigh wave dispersion.

3.2 Constant Length Fracture Distributions

In the following, we consider square samples with a side length of 50 cm drawn from the fractured granite formation (Figure 2). The fractures are represented as rectangular poroelastic features with an aperture of 0.4 mm and a length of 12 cm. We analyze the seismic response for fracture densities of 0.25%, 0.50%, and 0.75% for two end-member-type connectivities: (i) connected case, where all fractures have at least one connection with another fracture; (ii) unconnected case, where the fractures do not have any connections with each other. A single realization from each set of samples is illustrated in Figure 3. Recall that we infer effective body wave velocities for each fracture density and

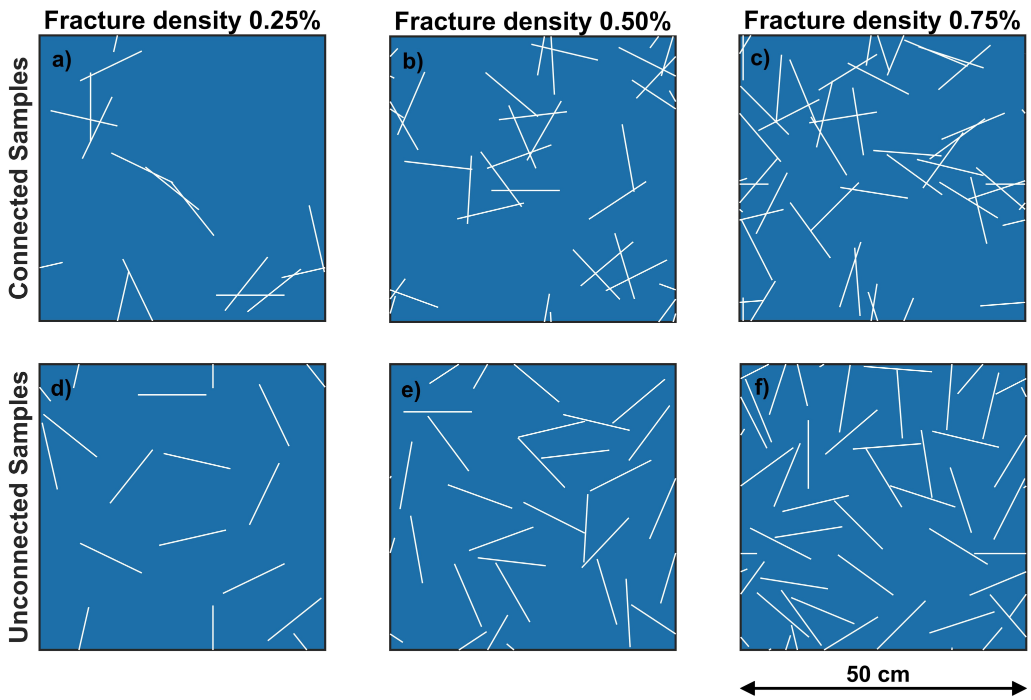

Figure 3. Examples of fracture distributions employed to derive effective body wave velocities of the fractured layer (Figure 2). We consider representative samples comprising (a, b, c) connected and (d, e, f) unconnected fracture distributions. Each column depicts a different fracture density: (a, d) 0.25%, (b, e) 0.50% and (c, f) 0.75%. The side length of the samples is 50 cm, and fractures are rectangular poroelastic features with a length of 12 cm and a width of 0.4 mm.

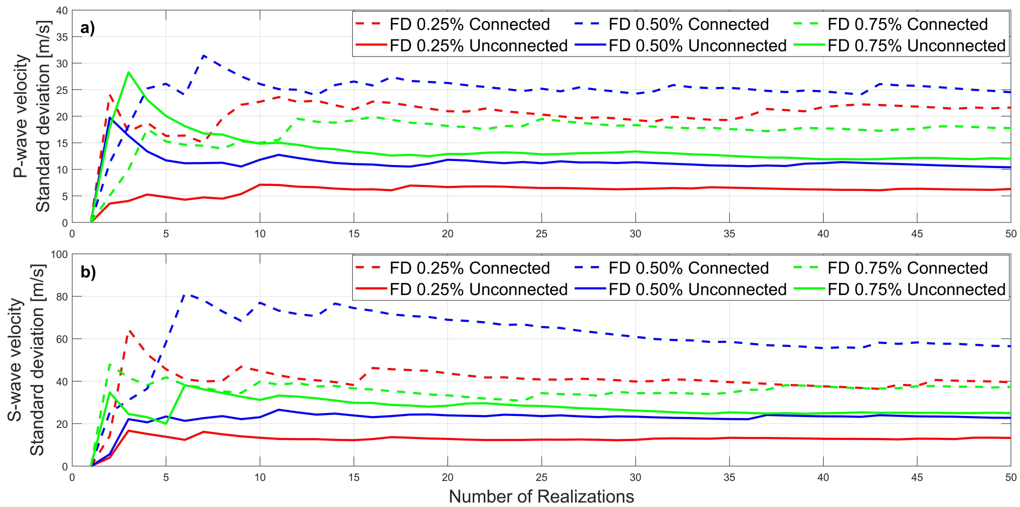

Figure 4. Standard deviations of (a) P- and (b) S-waves at 1 Hz as functions of the number of realizations for connected (dashed lines) and unconnected (solid lines) samples of constant fracture length and fracture densities of 0.25%, 0.50%, and 0.75%.

connectivity using a Monte Carlo approach. Figure 4 shows the results of the standard deviations as functions of the number of realizations for a frequency of 1 Hz, which is representative of Rayleigh wave studies and located within the non-dispersive plateau. We find that after 50 realizations, the standard deviations have stabilized and, thus, the average of the velocities of each sample set can be considered as being representative of the effective velocities of the corresponding fractured layers (Rubino et al., 2009).

Figure 5 shows the resulting effective P- and S-wave velocities as functions of frequency for the scenarios illustrated in Figure 3. In general, both P- and S-wave velocities decrease with increasing fracture densities. However, we observe that, when considering a constant fracture density, velocities for the unconnected case tend to be higher than those for the connected case. This velocity drop in presence of connected fractures, which is particularly prominent for frequencies around 1Hz, is due to FPD effects (Rubino et al., 2014, 2017). To reconcile this, it is important to account for the fact that, for such frequencies, there is not enough time in a half wave cycle to allow for hydraulic communication between fractures and background and, thus, fractures behave as hydraulically sealed. Therefore, in presence of unconnected fractures, there is a significant pressure buildup in the fluid contained in the fractures in response to the passage of seismic waves, which in turn, opposes the deformation. Conversely, in the presence of connected fractures, there is enough time for the fluid pressure within connected fractures to equilibrate, the stiffening effect of the fracture fluid is correspondingly diminished and, hence, the medium behaves as if it was softer, which manifests itself in the form of the observed velocity drop (Figure 5). It is interesting to observe in Figure 5 that the body wave velocity drop is more significant for the case of S-waves than for the P-waves. The reason for this is that, in the case of P-waves, regardless of the orientation, the fluid contained in a given fracture will experience a pressure increase in response to the associated compression. Conversely, in the case of S-waves, the associated deformation of the fractures increases the fluid pressure in some fractures and diminishes it in others, depending on their orientation with respect to the direction of propagation of the seismic perturbation (Rubino et al., 2017). This particularity, in turn, implies that in the presence of connected fractures, the local fluid pressure gradients may be significantly higher for S-waves than for P-waves. Consequently, the associated reduction of stiffening effects and, thus, the magnitude of the associated velocity drop is much more significant in the case of S-waves (Figure 5). These effects are accounted for in the model within the framework of poroelasticity. It is, however, important to remark that, for the range of frequencies usually employed for passive seismic surveys ($\sim$ 0.1 - 10 Hz) , dispersion in the resulting effective velocities is almost non-existent (Figure 5). We have verified that the residual P-wave dispersion in the considered frequency range has no noticeable effect on the simulations we performed. This allows, in turn, for the use of the upscaled effective body wave velocities to compute Rayleigh wave velocity dispersion curves employing an elastic model (Section 2). Table 2 summarizes the corresponding velocity values (Figure 5) which we consider in the following to study Rayleigh wave characteristics.

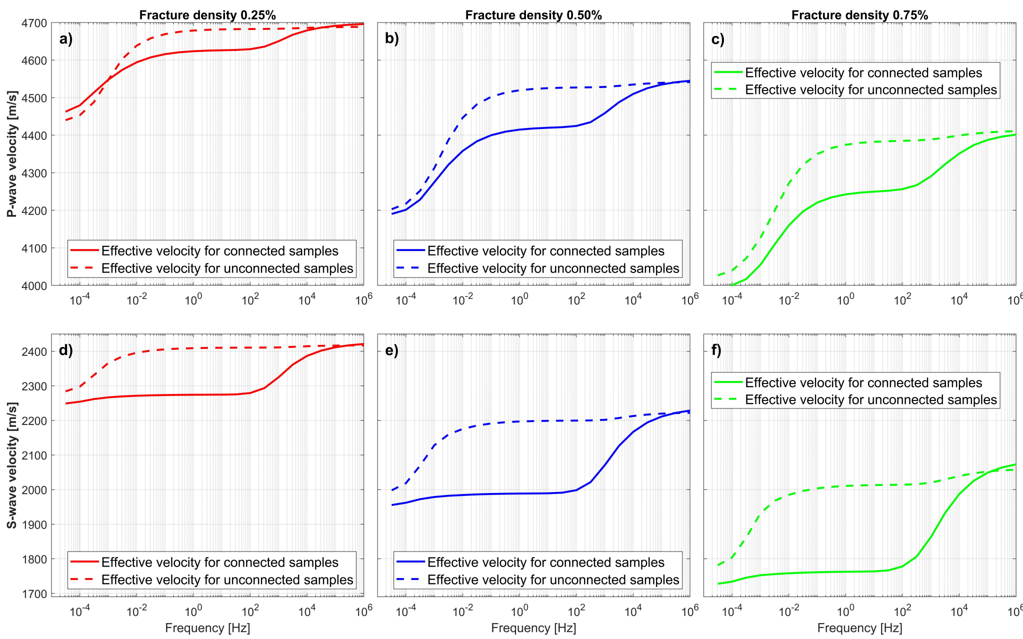

Figure 5. (a, b, c) Effective P- and (d, e, f) S-wave velocities inferred through a Monte Carlo approach for connected (solid lines) and unconnected (dashed lines) fractures of constant length and fracture densities of 0.25%, 0.50%, and 0.75%.

Table 2. Layer thicknesses and seismic properties of the considered model (Figure 2).

Lithology	Thickness [m]	V_P [m/s]	V_S [m/s]	ρ_b [kg/m^3]
Sandstone	2500	3500	2000	2500
Fractured granite	700	See Below	See Below	See Below
Intact granite	Infinite	4810	2620	2700

Properties of the fractured granite layer: constant length fracture distributions

Fracture density	Connectivity	V_P [m/s]	V_S [m/s]	ρ_b [kg/m^3]
0.25%	Connected	4623	2274	2694
0.25%	Unconnected	4679	2409	2694
0.50%	Connected	4415	1989	2690
0.50%	Unconnected	4520	2197	2690
0.75%	Connected	4242	1762	2687
0.75%	Unconnected	4374	2011	2687

Note. The properties corresponding to the fractured granite layer are depicted in the lower half of the table and result from taking the velocities corresponding to the non-dispersive plateau (Figure 5).

The Rayleigh phase and group velocities obtained for the canonical model are shown in Figure 2 and the different characteristics for the fracture network, summarized in Table 2, are shown in Figure 6. In general, there is a distinct phase velocity behaviour for all scenarios considered (Figures 6a to 6c). This is due to the fact that different frequencies are sensitive to different depths of investigation, with low frequencies being dominated by the properties of intact granite and high frequencies by those of sandstone. Sensitivity to the fractured granite layer prevails for frequencies between ∼0.1 Hz and ∼1 Hz. We note that differences between the Rayleigh wave phase velocities associated with the connected and unconnected cases increase with fracture density, which is expected from the body wave velocity results (Figure 5). We quantify the relative velocity variation, computed as the ratio between the differences and the average of the connected and unconnected case for each frequency (black dashed line in Figures 6 a to f). The peak of the relative difference curve for phase velocities occurs around 0.3 Hz, with values of 1%, 1.8%, and 2.7% for fracture densities of 0.25%, 0.50%, and 0.75%, respectively. Rayleigh wave group velocities (Figures 6 d to f) exhibit similar characteristics as the phase velocities. For intermediate frequencies, where the curves are sensitive to the fractured granite layer, we note that the relative differences for the group velocities are twice of the phase velocities, with a peak located near 0.25 Hz and a notch near 0.3 Hz. Peak relative difference values between the connected and unconnected cases are 2%, 3.8%, and 5.5% for fracture densities of 0.25%, 0.50% and 0.75%, respectively. These results indicate that, for the considered scenarios and for constant fracture lengths, both phase and group Rayleigh wave velocities are highly sensitive to changes in the fracture connectivity.

3.3 Stochastic Distribution of Fracture Lengths

As seen above, fracture connectivity greatly influences Rayleigh wave dispersion characteristics when the fracture lengths are constant. In the following, we consider a more realistic scenario based on a stochastic distribution of fracture lengths. Following pertinent previous works on this topic (e.g., de Dreuzy et al., 2001; Bonnet et al., 2001;

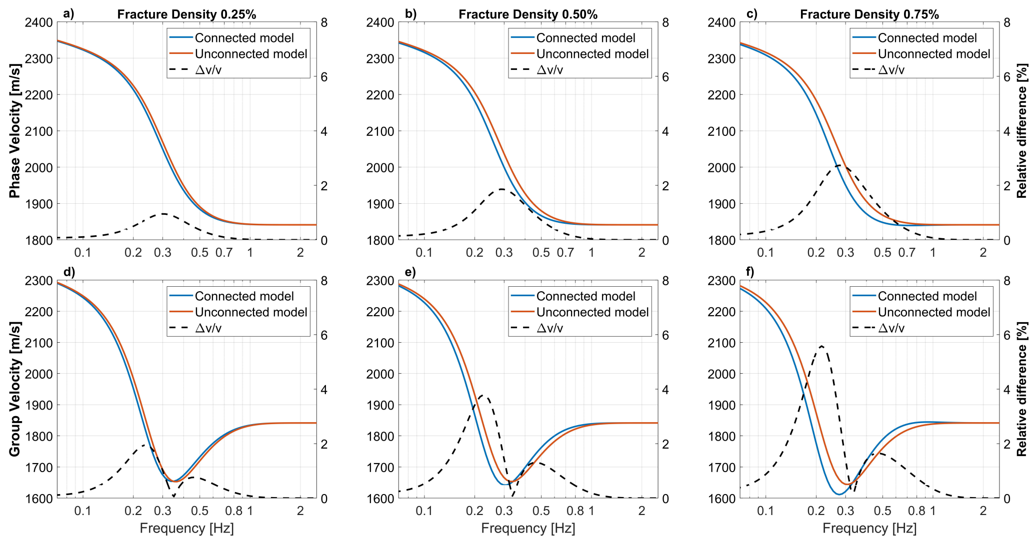

Figure 6. (a, b, c) Rayleigh wave phase and (d, e, f) group velocities for the connected (blue solid lines) and unconnected (orange solid lines) scenarios for different fracture densities. Given the small value of the absolute differences, we also illustrate relative velocity differences (dashed black lines) with scales depicted on the right-hand side of the corresponding plots. The latter are computed as the ratio between the differences and the average of the connected and unconnected case for each frequency.

Hunziker et al., 2018), we use a power law of the form

$$n(L) = f_d(a-1)\frac{L^{-a}}{L_{min}^{1-a}}; L \in [L_{min}, L_{max}], \tag{12}$$

where L is the fracture length, $n(L)$ is the number of fractures in the considered sample with a length comprised between L and $L+dL$, f_d is the fracture density, a is the characteristic exponent of the fracture size distribution, and L_{min} and L_{max} are the bounding minimum and maximum values of the distribution, respectively. While earlier works (e.g., de Dreuzy et al., 2001) consider fracture density as the number of fracture centers per area, Hunziker et al. (2018) defines it as the ratio of the fracture area over the total area of the studied medium. This allows to distinguish between the effects associated with changes of fracture volume and fracture length. The exponent a can take values between 1.5 and 3 and controls the prevalence of shorter to longer fractures within the limits given by L_{min} and L_{max}. For this work, we choose L_{min} and L_{max} as 4 cm and 25 cm, respectively. Together with a fixed aperture of 0.4 mm, results in fracture aspect ratios between 100 and 625, which is in agreement with corresponding observations of Vermilye and Scholz (1995) for real fractures. For the exponent a, we choose an intermediate value of 2.25, which implies that there is no predominance of neither shorter nor longer fractures on the seismic response of the medium (Hunziker et al., 2018).

The considered samples are generated in the same way as those characterized by constant length fractures and we employ the same physical properties for the fractures and background given in Table 1. Again, we consider three different fracture densities: 0.25%, 0.50%, and 0.75%, and two end-member-type connectivity scenarios of fully connected and fully unconnected fractures. Figure 7 illustrates some examples of the fracture distribution realizations considered in this section. We again employ the upscaling procedure described in section 2 in combination with a Monte Carlo approach to obtain the effective mechanical properties of the fractured formation. Although not shown here for brevity, we found that 50 samples are sufficient to obtain a stable standard deviation and, thus, representative body wave velocities.

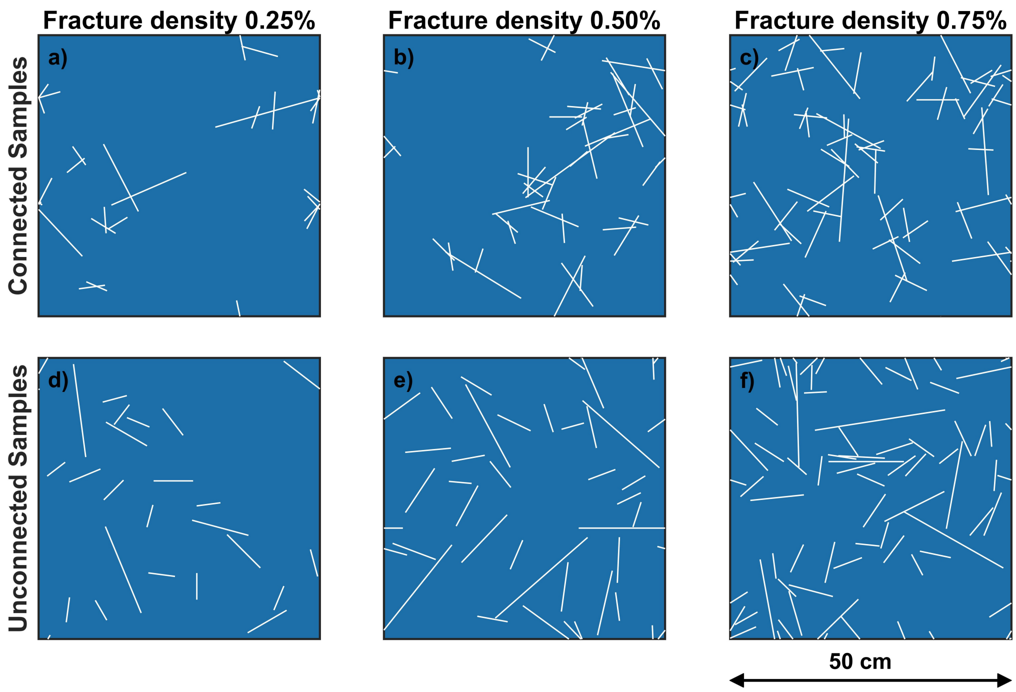

Figure 7. Examples of the variable length fracture distributions employed to derive the effective body wave velocities of fractured granite. We consider representative samples comprising (a, b, c) connected and (d, e, f) unconnected fractures. Each column depicts a different fracture density: (a, d) 0.25%, (b, e) 0.50%, and (c, f) 0.75%. Samples have a 50 cm side length. Fractures are rectangular features with a constant aperture of 4 mm and length drawn from a power law distribution (Equation 12).

Table 3. Properties of the fractured granite layer: Variable length fractures distributions

Fracture density	Connectivity	V_P [m/s]	V_S [m/s]	ρ_b [kg/m^3]
0.25%	Connected	4661	2337	2694
0.25%	Unconnected	4701	2445	2694
0.50%	Connected	4477	2093	2690
0.50%	Unconnected	4551	2265	2690
0.75%	Connected	4310	1855	2687
0.75%	Unconnected	4416	2093	2687

Note. Characteristics of the fractured layer schematically illustrated in Figure 2 used for computing Rayleigh wave dispersion curves.

The results for the effective P- and S-body wave velocities as functions of frequency are shown in Figure 8. The characteristics of the velocity dispersion curves are similar to those for the constant fracture length scenario (Figures 6 and 8). Each fracture density shows the manifestations of FPD effects described in section 2, with a constant velocity plateau for the frequencies of interest between $\sim$0.01 and $\sim$3 Hz. We note that velocities for P-waves (Figures 8a to 8c) and S-waves (Figures 8d to 8f) decrease for increasing fracture density. As observed previously the difference in body wave velocities between connected and unconnected fracture distributions increases for larger fracture densities and is more prominent for S-waves than for P-waves. This indicates that, regardless of the fracture length distribution, velocity variations associated with changes in fracture connectivity are strongly affected by the fracture density. The resulting effective velocities for each scenario are listed in Table 3.

Figure 9 illustrates the Rayleigh wave velocity dispersion for the variable fracture length case. Phase and group velocities present limiting values at high and low frequencies corresponding to the values of sandstone and intact granite, respectively. Sensitiv-

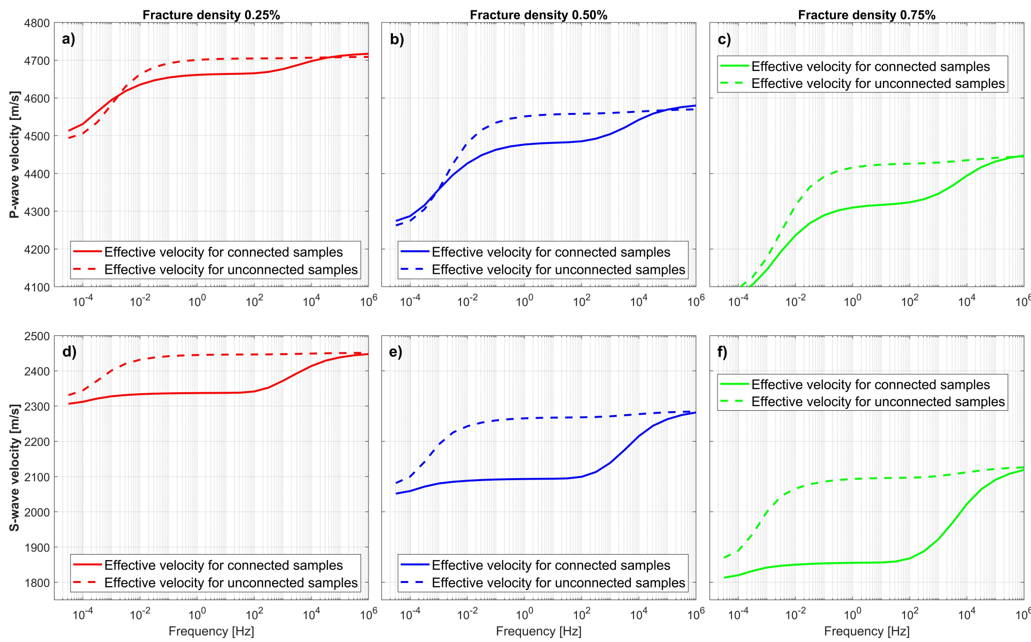

Figure 8. (a, b, c) Effective P- and (d, e, f) S-wave velocities for connected (solid lines) and unconnected (dashed lines) fractures of variable lengths (Figure 7). We illustrate the results for fracture densities of 0.25%, 0.50%, and 0.75%. The curves are obtained by averaging the responses of 50 fracture network realizations.

ity to the fractured layer prevails at frequencies between ∼0.1 Hz and ∼1 Hz. For Rayleigh wave phase velocities (Figures 9a to 9c), the maximum of the relative difference between connected and unconnected cases occurs near 0.3 Hz with values of 0.7%, 1.4%, and 2.3% for fracture densities of 0.25%, 0.50%, and 0.75%, respectively. For Rayleigh wave group velocities, maximum relative differences occur for a frequency close to 0.25 Hz with values of 1.5%, 2.9%, and 4.8% for fracture densities of 0.25%, 0.50%, and 0.75%, respectively. A comparison of Rayleigh wave velocities for the variable length case with the corresponding results obtained for the constant length fracture distributions show that the relative differences for the latter case are approximately 25% higher. However, the relative effect of changing fracture density or connectivity is the same for both variable and constant length fracture distributions. This implies that for the fracture length variations considered in this work, the controlling factors regarding FPD effects on Rayleigh waves are the fracture density and fracture connectivity rather than the length distribution of the fractures.

In order to obtain a clearer idea on the impact of FPD effects on Rayleigh wave dispersion, we repeat the analysis for additional values of fracture density ranging between 0.25% and 0.90% (Figure 10). Figures 10a and 10b show the results of the effective body wave velocities for a frequency of 1 Hz, which is representative of the non-dispersive plateau (dashed lines). In addition to the connected and unconnected scenarios, we also consider samples which have not been subjected to the previously outlined control of connectivity and, hence, have not undergone any fracture substitution. We refer to this case as randomly connected. As the end-member-type cases of fully connected and fully unconnected distributions are not likely to occur in real formations, the randomly connected scenario is expected to be more representative of the naturally-occurring degree of connectivity for a given fracture density. We again observe a clear trend of decreasing P- and S-wave velocities with increasing fracture density (Figures 10a and 10b). In particular, we observe that for a given fracture density, connected fracture distributions have the lowest velocities, unconnected fracture distributions have the highest velocities, and

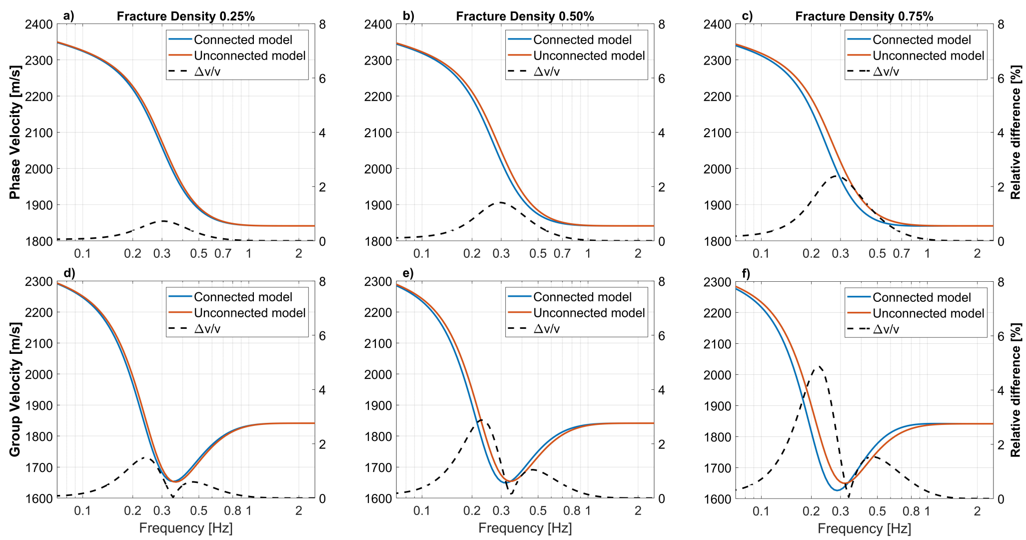

Figure 9. (a, b, c) Rayleigh wave phase and (d, e, f), group velocities for connected (blue solid lines) and unconnected (orange solid lines) fractures whose length distribution obey the power law given in Equation 12 (Figure 7). Dashed black lines indicate the relative velocity difference, computed as the ratio between the differences and the average of the connected and unconnected case for each frequency.

randomly connected fracture distributions (red dashed lines) have intermediate velocities. The velocities of the randomly connected fracture distributions are closer to those of the unconnected fracture distributions for lower fracture densities and closer to those of connected fracture network for higher fracture densities. This is expected as the probability of interconnections increases with the fracture density.

Figures 10a and 10b also show the velocities in the high-frequency or no-flow limit at 10^6 Hz, which corresponds to the elastic behaviour of the samples (solid lines). We observe that, while the trend of decreasing velocity with increasing fracture density is still present, the effect of fracture connectivity is largely negligible. This is consistent with works based on elastic approximations of fractured media (e.g., Grechka & Kachanov, 2006), where FPD effects are neglected and, thus, suggest that fracture connectivity has no impact on the mechanical properties. Interestingly, P- and S-wave velocities for the randomly connected case considering FPD effects (red dashed lines) decreases more drastically with the fracture density than the corresponding high frequency estimates (red solid lines). Figures 10c and 10d show the maximum relative Rayleigh wave velocity difference between connected and unconnected fractures for a given fracture density in the presence and absence of FPD. For the cases considering FPD effects, this corresponds to the analysis shown in Figure 9 extended for additional fracture densities. For the cases disregarding FPD effects, the relative difference corresponds to velocities in the high-frequency no-flow limit (10^6 Hz). Figure 10c corresponds to the maximum relative difference between connected and unconnected fracture distributions for Rayleigh wave group velocity, at a frequency of $\sim$0.2 Hz, and Figure 10d shows the maximum relative difference for Rayleigh wave phase velocity, at a frequency of $\sim$0.3 Hz. We note that, when considering FPD effects, the difference between connected and unconnected cases is already significant for lower fracture densities and increases progressively with increasing fracture density. Conversely, in the absence of FPD effects, the difference between the connected and unconnected cases remains largely negligible for all fracture densities considered. Overall, these results suggest that disregarding FPD effects in a velocity analysis, that is, considering the high frequency elastic representation, may lead to an overestimation of the fracture density changes required to explain a given velocity change.

Finally, we consider variations in the thickness and the depth of the fractured granite layer in our canonical model (Figure 2, Table 2) in order to assess whether and to what extent such changes affect the sensitivity to variations in fracture connectivity. Figure 11 shows the effects of varying the depth and thickness of the fractured layer for a fracture density of 0.50% (Table 3). Figures 11a and 11d document the Rayleigh wave phase and group velocities after increasing the thickness of the surficial sandstone layer from 2500 m to 3500 m, while keeping the thickness of the fractured layer unchanged. Figures 11b and 11e show the results for reference model without modifications. For a deeper location of the fractured layer (Figures 11a and 11d), we observe that the maximum relative differences between the connected and unconnected cases shift towards lower frequencies, as longer wavelengths are sensitive to greater depths. We also see that the magnitude of the relative difference decreases, as the increase of the thickness of the overlaying formation diminishes the impact of the reservoir on the Rayleigh wave dispersion. Figures 11c and 11f show the results after reducing the thickness of the fractured layer from 700 m to 350 m. We observe no appreciable frequency shift but there is, as expected, an important decrease of the relative differences, which, nevertheless, remain relevant when compared to corresponding field evidence (e.g., Obermann et al., 2015; Taira et al., 2018).

4 Discussion

We employed a numerical upscaling procedure based on the assumption of quasi-static poroelasticity, which does not account for inertial effects to obtain the effective body wave velocities of fractured samples. The transition frequency, at which inertial effects become relevant, depends on the material properties. For all scenarios of practical interest in the given context, this frequency is much higher than the frequency range used in passive seismic exploration in general and Rayleigh wave studies in particular and,

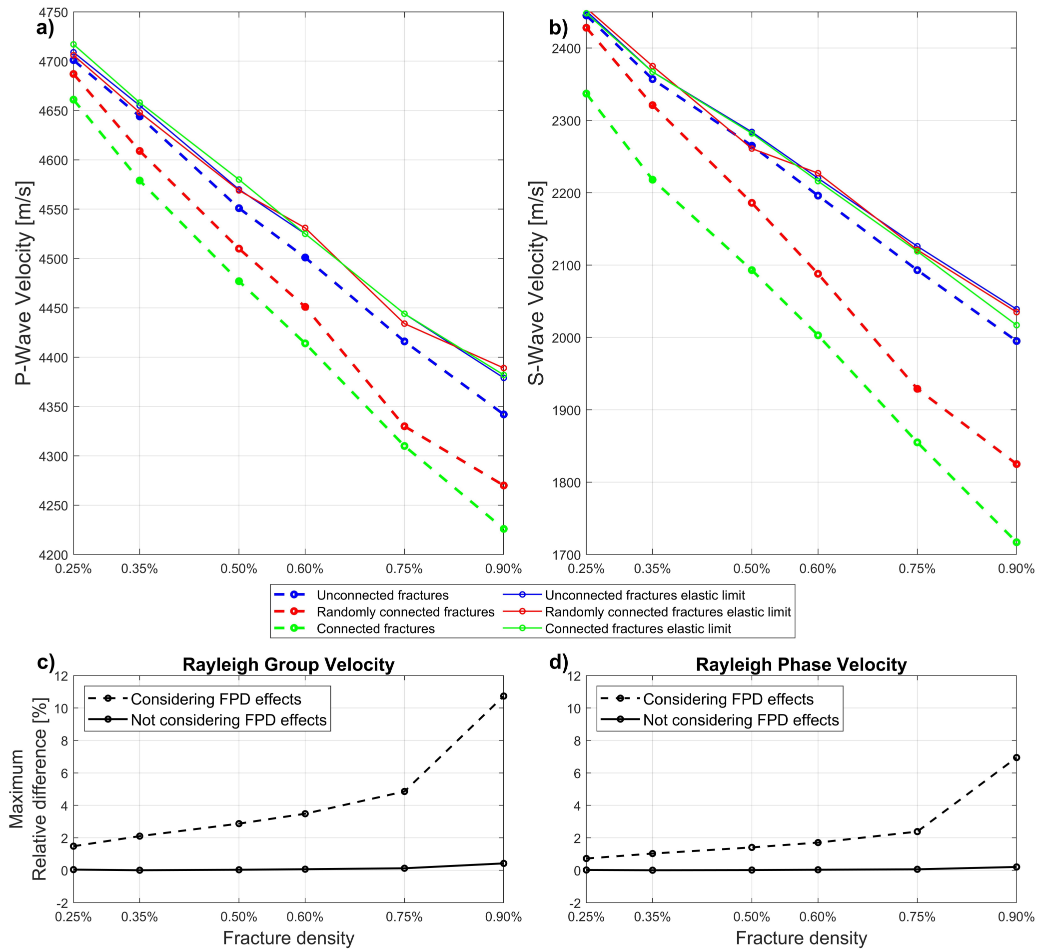

Figure 10. (a) Effective P- and (b) S-wave velocities as functions of fracture density for different degrees of fracture connectivity considering a stochastic distribution of the fracture lengths (Equation 12, Figure 7). Dashed lines correspond to a frequency of 1 Hz, which is representative for passive seismic studies, while solid lines are computed using a frequency of 10^6 Hz, thus resulting in elastic behaviour of the probed samples. Maximum relative difference for (c) Rayleigh wave group and (d) phase velocities between the connected and unconnected distributions computed for the elastic and poroelastic scenarios.

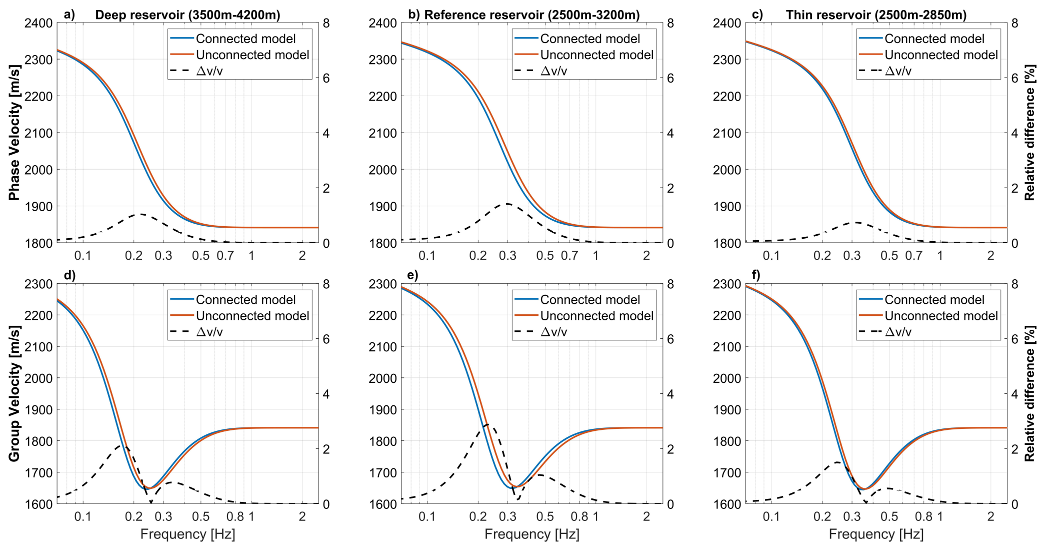

Figure 11. Effects of variations in the depth and thickness of the fractured layer in our canonical model (Figure 2, Table 2) for a fracture density of 0.50% and considering a stochastic distribution of lengths (Equation 12, Figure 7). (b, e) Phase and group velocities for the reference case (Table 3). Phase and group velocities (a, d) when the fractured layer is located 1000 m deeper and (c, f) for fractured layer with a thickness of 350 m as compared to one of 700 m used for the reference model.

hence, the poroelastic upscaling procedure used in this study is valid as long as fracture sizes remain much smaller than the predominant wavelength.

The observed fracture connectivity effects on Rayleigh wave velocities are significantly higher than the velocity variations reported from passive seismic monitoring of geothermal sites (Obermann et al., 2015; Taira et al., 2018). This is likely due to the fact that in a natural environment, changes of fracture connectivity are likely to be small and gradual, while we are considering the end-member scenarios of entirely unconnected and connected fracture networks. Moreover, 2D simulations tend to overestimate FPD effects on the seismic response of the samples (Hunziker et al., 2018). Another point of discrepancy may be the thickness of the fractured reservoir of our model, as natural and enhanced fractured reservoirs are likely to be thinner than 700 m. In addition, to compute Rayleigh wave dispersion curves, we adopted a model consisting of isotropic and homogeneous layers. It is known that in the case of fractures with preferential orientations, FPD effects have significant impact on the velocity anisotropy of the probed samples (Rubino et al., 2017). The corresponding effects in surface wave dispersion, in addition to more complex model geometries including lateral variations of the material properties and layer thicknesses should be addressed in future works.

We also considered distributions of fractures with constant aperture and material properties, and while the resulting aspect ratio distribution of the fractures is realistic (e.g., Vermilye & Scholz, 1995), the length variation ranges and sample sizes are governed by computational constraints. This raises the question regarding the scalability and relevance of our results for realistic fractures, which can be several orders-of-magnitude larger than the ones considered in our samples. Following the work of Guo et al. (2017), which considers fracture networks composed by two sets of orthogonal equal fractures, the characteristic frequency of FB-FPD, F_{fb}, can be expressed as

$$F_{fb} = \frac{8D_b}{a_f^2}, \tag{13}$$

where a_f denotes the length of the fractures and D_b the diffusivity of the background medium. D_b is expressed as

$$D_b = \frac{M_b L_b \kappa_b}{\eta L_b^{sat}}, \tag{14}$$

where M_b corresponds to the fluid storage coefficient of the background material, L_b and L_b^{sat} are the P-wave moduli for the dry and saturated cases, respectively, κ_b is the permeability and η is the fluid viscosity. As background properties are not affected by changes in fracture size, F_{fb} is expected to decrease for increasing fracture size (Equation 13). On the other hand, the characteristic frequency of FF-FPD effects, F_{ff}, corresponding to the maximum attenuation and dispersion due to this process, is given by (Guo et al., 2017)

$$F_{ff} = \frac{8D_e}{a_f^2}, \tag{15}$$

where D_e denotes the diffusivity of an effective medium, which considers the fractures as the pore space and the background as the solid phase. D_e is expressed as

$$D_e = \frac{M_e L_e \kappa_{fr} f_d}{\eta L_e^{sat}}, \tag{16}$$

where M_e corresponds to the effective medium fluid storage coefficient, L_e and L_e^{sat} are the P-wave moduli for the dry and saturated effective medium, respectively, κ_{fr} is the permeability of the fractures and f_d is the fracture density. As can be seen in Equations 15 and 16, F_{ff} depends on the effective medium diffusivity and the fracture size. Neglecting possible changes in elastic properties of the fractures and considering that an increase in fracture length is associated with an increase in aperture (e.g., Vermilye & Scholz, 1995) and, therefore, in permeability (e.g., Brown, 1987), it can be shown that the impact of fracture size on F_{ff} tends to be counteracted by the associated increase in permeability. For this reason, we expect that the FF-FPD characteristic frequency will not be significantly affected by the scale of the fractures. This, together with the fact that F_{fb} decreases with increasing fracture size implies that the frequencies typically employed in ambient seismic noise studies are likely to remain in the non-dispersive plateau. This, in turn, suggests that the effects of connectivity are expected to remain significant regardless of the scale of the fractures considered. However, further work is required in this direction to assess associated scaling characteristics for complex fracture distributions and possible fracture compliance changes with scale. This would allow to evaluate the corresponding impact not only on the characteristic frequencies but also on the magnitude of the fracture connectivity effects.

5 Conclusions

We have employed a numerical upscaling procedure together with a Monte Carlo approach to obtain effective body wave velocities of a fractured formation. This approach allows to account for FPD effects between fractures and their embedding background as well as between connected fractures. For the frequency range typical of ambient seismic noise analysis, we have found that there is no body wave velocity dispersion or attenuation due to FPD effects for our models. However, the presence of interconnections between fractures produces a significant drop of the body wave velocities in comparison with the corresponding unconnected scenario. This is an important poroelastic phenomenon, which is generally referred to as pore fluid softening/stiffening and which cannot be explained from a purely elastic perspective. The effective body wave velocities we obtained were employed to determine the effects of fracture connectivity on Rayleigh wave phase and group velocities. Based on the prevailing elastic models, changes in Rayleigh velocities in fractured environments were so far largely attributed to changes in fracture density or aperture. Our results indicate that fracture connectivity plays an important role in the seismic response of fractured formations due to FPD effects and that these effects are appreciable when performing Rayleigh wave dispersion analysis.

We compared the results from distributions with constant fracture lengths and fracture lengths drawn from a power law distribution. We found that, for the range of length variations employed, fracture length distribution seems to be of subordinate importance with respect to changes in connectivity or fracture density. Our results demonstrate the importance of FPD effects for Rayleigh waves in fractured media, and notably, that neglecting FPD effects between connected fractures may lead to an overestimation of fracture density.

Acknowledgments

The data set used to plot the Figures presented in this paper can be downloaded from https://doi.org/10.5281/zenodo.4788646. This work is supported by grant number 200020-178946 from the Swiss National Science Foundation and was in part completed within the Swiss Competence Center on Energy Research - Supply of Electricity, with the support of Innosuisse. J. G. R. gratefully acknowledges the financial support received from the Agencia Nacional de Promoción Científica y Tecnológica of Argentina (PICT 2017-2976).

References

Aki, K., & Lee, W. (1976). Determination of three-dimensional velocity anomalies under a seismic array using first P arrival times from local earthquakes: 1. A homogeneous initial model. *Journal of Geophysical research*, *81*(23), 4381–4399.

Aki, K., & Richards, P. G. (1980). *Quantitative Seismology: Theory and Practice.* New York: W.H. Freeman.

Biot, M. A. (1941). General theory of three-dimensional consolidation. *Journal of Applied Physics*, *12*(2), 155–164.

Biot, M. A. (1956a). Theory of propagation of elastic waves in a fluid-saturated porous solid. II. Higher frequency range. *The Journal of the Acoustical Society of America*, *28*(2), 179–191.

Biot, M. A. (1956b). Theory of propagation of elastic waves in a fluid-saturated porous solid. I. Low-frequency range. *The Journal of the Acoustical Society of America*, *28*(2), 168–178.

Biot, M. A. (1962). Mechanics of deformation and acoustic propagation in porous media. *Journal of Applied Physics*, *33*(4), 1482–1498.

Bonnet, E., Bour, O., Odling, N. E., Davy, P., Main, I., Cowie, P., & Berkowitz, B. (2001). Scaling of fracture systems in geological media. *Reviews of Geophysics*, *39*(3), 347–383.

Boullenger, B., Verdel, A., Paap, B., Thorbecke, J., & Draganov, D. (2015). Studying CO 2 storage with ambient-noise seismic interferometry: A combined numerical feasibility study and field-data example for Ketzin, Germany. *Geophysics*, *80*(1), Q1–Q13.

Brenguier, F., Shapiro, N. M., Campillo, M., Ferrazzini, V., Duputel, Z., Coutant, O., & Nercessian, A. (2008). Towards forecasting volcanic eruptions using seismic noise. *Nature Geoscience*, *1*(2), 126–130.

Brown, S. R. (1987). Fluid flow through rock joints: the effect of surface roughness. *Journal of Geophysical Research: Solid Earth*, *92*(B2), 1337–1347.

Buchen, P., & Ben-Hador, R. (1996). Free-mode surface-wave computations. *Geophysical Journal International*, *124*(3), 869–887.

Calò, M., Kinnaert, X., & Dorbath, C. (2013). Procedure to construct three-dimensional models of geothermal areas using seismic noise cross-correlations: application to the Soultz-sous-Forêts enhanced geothermal site. *Geophysical Journal International*, *194*(3), 1893–1899.

Campillo, M., & Paul, A. (2003). Long-range correlations in the diffuse seismic coda. *Science*, *299*(5606), 547–549.

de Dreuzy, J.-R., Davy, P., & Bour, O. (2001). Hydraulic properties of two-dimensional random fracture networks following a power law length distribution: 1. Effective connectivity. *Water Resources Research*, *37*(8), 2065–2078.

Detournay, E., & Cheng, A. H.-D. (1993). Fundamentals of poroelasticity. In C. Fairhurst (Ed.), *Analysis and design methods* (pp. 113–171). Oxford: Pergamon.

Favino, M., Hunziker, J., Caspari, E., Quintal, B., Holliger, K., & Krause, R. (2020).

Fully-automated adaptive mesh refinement for media embedding complex heterogeneities: application to poroelastic fluid pressure diffusion. *Computational Geosciences*, *24*(3), 1101–1120.

Gassenmeier, M., Sens-Schönfelder, C., Delatre, M., & Korn, M. (2014). Monitoring of environmental influences on seismic velocity at the geological storage site for CO_2 in Ketzin (Germany) with ambient seismic noise. *Geophysical Journal International*, *200*(1), 524–533.

Gassmann, F. (1951). Elasticity of porous media. *Vierteljahrsschrder Naturforschenden Gesselschaft*, *96*(1–23).

Grechka, V., & Kachanov, M. (2006). Effective elasticity of rocks with closely spaced and intersecting cracks. *Geophysics*, *71*(3), D85–D91.

Guo, J., Rubino, J. G., Glubokovskikh, S., & Gurevich, B. (2017). Effects of fracture intersections on seismic dispersion: theoretical predictions versus numerical simulations. *Geophysical Prospecting*, *65*(5), 1264–1276.

Gurevich, B., Brajanovski, M., Galvin, R. J., Müller, T. M., & Toms-Stewart, J. (2009). P-wave dispersion and attenuation in fractured and porous reservoirs–poroelasticity approach. *Geophysical Prospecting*, *57*(2), 225–237.

Haskell, N. A. (1953). The dispersion of surface waves on multilayered media. *Bulletin of the seismological Society of America*, *43*(1), 17–34.

Hunziker, J., Favino, M., Caspari, E., Quintal, B., Rubino, J. G., Krause, R., & Holliger, K. (2018). Seismic attenuation and stiffness modulus dispersion in porous rocks containing stochastic fracture networks. *Journal of Geophysical Research: Solid Earth*, *123*(1), 125–143.

Mavko, G., Mukerji, T., & Dvorkin, J. (1998). *The Rock Physics Handbook*. New York: Cambridge University Press.

Milani, M., Rubino, J. G., Müller, T. M., Quintal, B., Caspari, E., & Holliger, K. (2016). Representative elementary volumes for evaluating effective seismic properties of heterogeneous poroelastic media. *Geophysics*, *81*(2), D169–D181.

Nakagawa, S., & Schoenberg, M. A. (2007). Poroelastic modeling of seismic boundary conditions across a fracture. *The Journal of the Acoustical Society of America*, *122*(2), 831–847.

Obermann, A., Kraft, T., Larose, E., & Wiemer, S. (2015). Potential of ambient seismic noise techniques to monitor the St. Gallen geothermal site (Switzerland). *Journal of Geophysical Research: Solid Earth*, *120*(6), 4301–4316.

Obermann, A., Planès, T., Larose, E., & Campillo, M. (2013). Imaging preeruptive and coeruptive structural and mechanical changes of a volcano with ambient seismic noise. *Journal of Geophysical Research: Solid Earth*, *118*(12), 6285–6294.

Planès, T., Obermann, A., Antunes, V., & Lupi, M. (2020). Ambient-noise tomography of the greater geneva basin in a geothermal exploration context. *Geophysical Journal International*, *220*(1), 370–383.

Press, W. H., William, H., Teukolsky, S. A., Saul, A., Vetterling, W. T., & Flannery, B. P. (1986). *Numerical Recipes: The Art of Scientific Computing*. New York: Cambridge University Press.

Rubino, J. G., Caspari, E., Müller, T. M., & Holliger, K. (2017). Fracture connectivity can reduce the velocity anisotropy of seismic waves. *Geophysical Journal International*, *210*(1), 223–227.

Rubino, J. G., Caspari, E., Müller, T. M., Milani, M., Barbosa, N. D., & Holliger, K. (2016). Numerical upscaling in 2-D heterogeneous poroelastic rocks: Anisotropic attenuation and dispersion of seismic waves. *Journal of Geophysical Research: Solid Earth*, *121*(9), 6698–6721.

Rubino, J. G., Guarracino, L., Müller, T. M., & Holliger, K. (2013). Do seismic waves sense fracture connectivity? *Geophysical Research Letters*, *40*(4), 692–696.

Rubino, J. G., Müller, T. M., Guarracino, L., Milani, M., & Holliger, K. (2014). Seismoacoustic signatures of fracture connectivity. *Journal of Geophysical*

Research: Solid Earth, *119*(3), 2252–2271.

Rubino, J. G., Ravazzoli, C. L., & Santos, J. E. (2009). Equivalent viscoelastic solids for heterogeneous fluid-saturated porous rocks. *Geophysics*, *74*(1), N1–N13.

Shapiro, N. M., & Campillo, M. (2004). Emergence of broadband Rayleigh waves from correlations of the ambient seismic noise. *Geophysical Research Letters*, *31*(7).

Silver, P. G., Daley, T. M., Niu, F., & Majer, E. L. (2007). Active source monitoring of cross-well seismic travel time for stress-induced changes. *Bulletin of the Seismological Society of America*, *97*(1B), 281–293.

Socco, L., Foti, S., & Boiero, D. (2010). Surface-wave analysis for building near-surface velocity models — Established approaches and new perspectives. *Geophysics*, *75*, 91-110.

Solazzi, S. G., Hunziker, J., Caspari, E., Rubino, J. G., Favino, M., & Holliger, K. (2020). Seismic signatures of fractured porous rocks: the partially saturated case. *Journal of Geophysical Research: Solid Earth*, *125*(8), e2020JB019960.

Solazzi, S. G., Rubino, J., Müller, T. M., Milani, M., Guarracino, L., & Holliger, K. (2016). An energy-based approach to estimate seismic attenuation due to wave-induced fluid flow in heterogeneous poroelastic media. *Geophysical Journal International*, *207*(2), 823–832.

Stein, S., & Wysession, M. (2003). *An introduction to seismology, earthquakes, and earth structure.* Malden: Blackwell.

Taira, T., Brenguier, F., & Kong, Q. (2015). Ambient noise-based monitoring of seismic velocity changes associated with the 2014 Mw 6.0 South Napa earthquake. *Geophysical Research Letters*, *42*(17), 6997–7004.

Taira, T., Nayak, A., Brenguier, F., & Manga, M. (2018). Monitoring reservoir response to earthquakes and fluid extraction, Salton Sea geothermal field, California. *Science Advances*, *4*(1), e1701536.

Thomson, W. T. (1950). Transmission of elastic waves through a stratified solid medium. *Journal of Applied Physics*, *21*(2), 89–93.

Thurber, C. H. (1983). Earthquake locations and three-dimensional crustal structure in the Coyote Lake area, central California. *Journal of Geophysical Research: Solid Earth*, *88*(B10), 8226–8236.

Vermilye, J. M., & Scholz, C. H. (1995). Relation between vein length and aperture. *Journal of Structural Geology*, *17*(3), 423–434.

Vinci, C., Renner, J., & Steeb, H. (2014). On attenuation of seismic waves associated with flow in fractures. *Geophysical Research Letters*, *41*(21), 7515–7523.

Wang, Q.-Y., & Yao, H. (2020). Monitoring of velocity changes based on seismic ambient noise: A brief review and perspective. *Earth and Planetary Physics*, *4*(5), 532–542.